

Ice Ic without stacking disorder

by evacuating hydrogen from hydrogen hydrate

Kazuki Komatsu^{1*}, Shinichi Machida², Fumiya Noritake^{3,4}, Takanori Hattori⁵, Asami Sano-Furukawa⁵, Ryo Yamane¹, Keishiro Yamashita¹ & Hiroyuki Kagi¹

¹Geochemical Research Center, Graduate School of Science, The University of Tokyo, 7-3-1 Hongo, Bunkyo-ku, Tokyo 113-0033, Japan

²Neutron Science and Technology Center, CROSS, 162-1 Shirakata, Tokai, Naka, Ibaraki 319-1106, Japan

³Graduate Faculty of Interdisciplinary Research, University of Yamanashi, 4-3-11 Takeda, Kofu, Yamanashi 400-8511, Japan

⁴Computational Engineering Applications Unit, RIKEN, 2-1 Hirosawa, Wako, Saitama 351-0198, Japan

⁵J-PARC Center, Japan Atomic Energy Agency, 2-4 Shirakata, Tokai, Naka, Ibaraki 319-1195, Japan

*Corresponding author

e-mail: kom@eqchem.s.u-tokyo.ac.jp

Water freezes below 0 °C at ambient pressure, ordinarily to ice Ih with an ABAB... hexagonal stacking sequence. However, it is also known to produce “ice Ic” nominally with an ABCABC... cubic stacking sequence under certain conditions¹, and its existence in Earth’s atmosphere²⁻⁴, or in comets^{5,6} is debated. “Ice Ic”, or called as cubic ice, was first identified in 1943 by König⁷, who used electron microscopy to study the condensation of ice from water vapor to a cold substrate. Subsequently, many different routes to “ice Ic” have been established, such as the dissociation of gas hydrates, warming amorphous ices or annealing high-pressure ices recovered at ambient pressure, freezing of μ - or nano-confined water (see refs in ¹). Despite the numerous studies on “ice Ic”, its structure has not been fully verified, because the diffraction patterns of “ice Ic” show signatures of stacking-disorder^{1,8}, and ideal ice Ic without stacking-disorder had not been formed until very recently⁹. Here we demonstrate a route to obtain ice Ic without stacking-disorder by degassing hydrogen from the high-pressure form of hydrogen hydrate, C₂, which has a host framework that is isostructural with ice Ic¹⁰. Surprisingly, the stacking-disorder free ice Ic is formed from C₂ via an intermediate amorphous or nano-crystalline form under decompression, unlike the direct transformations that occur in the cases of recently discovered ice XVI¹¹ from neon hydrate, or ice XVII¹² from hydrogen hydrate. The obtained ice Ic shows remarkable thermal stability until the phase transition to ice Ih at 250 K; this thermal stability originates from the lack of dislocations, which promote changes in the stacking sequence¹³. This discovery of ideal ice Ic will promote understanding of the role of stacking-disorder¹⁴ on the physical properties of ice as a counter end-member of ice Ih.

“Ice Ic” is known as a metastable form of ice at atmospheric pressure. The routes to synthesize “ice Ic” are increasing steadily¹, and there is a consensus that it is possibly present during the first stage in ice formation in clouds¹⁵. Recent computer simulations suggest that even stacking-disordered “ice Ic”, called ice Isd⁸, could be the stable phase for crystallites up to sizes of at least 100,000 molecules¹⁴. The stability of stacking-disordered ices is extremely important because of the ubiquitous nature of ice. Stacking-disordered ice can be characterized by the degree of ice “cubicity”, χ , which can be defined as the fraction of cubic layers if the stacking is random^{1,8,16-18}. Until very recently, the highest cubicity was limited to $\sim 80\%$ ^{8,15}, but it has been reported that ideal ice Ic with 100% cubicity has been obtained by annealing ice XVII⁹.

From recent discoveries of polymorphs of ice XVI¹¹ and ice XVII^{12,19}, we hypothesized that ideal ice Ic could be obtained by degassing hydrogen from hydrogen hydrate, C₂. Five different phases in the H₂-H₂O system have been reported to date (see refs in ²⁰): Among them, neutron diffraction experiments have never been conducted for the higher-pressure phases, C₁ and C₂, probably due to the technical difficulty in loading hydrogen into a pressure vessel, or compressing it to pressures in the giga-pascal range. To synthesize ideal ice Ic, decompression under low-temperature conditions for degassing is necessary, which is also not straight-forward using conventional pressure-temperature controlling systems. We have developed a ‘Mito system’²¹, and have overcome these technical difficulties (see details in Methods).

We started by using a mixture of D₂O and MgD₂, which is an internal deuterium source, to synthesize hydrogen hydrate, C₂. After loading the mixture into a pressure-temperature controlling system, MgD₂ was decomposed by heating at 403 K and at ca. 0 GPa for 1 h through a nominal reaction of $\text{MgD}_2 + 3\text{D}_2\text{O} \rightarrow \text{Mg(OD)}_2 + 2\text{D}_2 + \text{D}_2\text{O}$ (at *b* in Fig. 1, the observed neutron diffraction patterns are shown in Extended Data Fig. 1). Then, the samples were cooled to room temperature (at *c* in Fig. 1) and typically compressed up to approximately 3 GPa until a C₂ phase was observed (at *d* in Fig. 1).

The neutron diffraction pattern for the C₂ phase obtained at 3.3 GPa and 300 K (at *d* in Fig. 1) was analyzed by the Rietveld method. We adopted a splitting site model for guest D atoms

located at the $48f$ site ($x, 1/8, 1/8$), and the host structure was identical to ice Ic¹⁷ ($Fd\bar{3}m$, O at the $8b$ site ($3/8, 3/8, 3/8$), D at the $32e$ site (x, x, x)). The calculated diffraction pattern was in good agreement with the observed one, as shown in Fig. 2a. The refined structural parameters are listed in Extended Data Table 1.

The sample was then cooled from 300 K to 100 K at around 3 GPa (path $d \rightarrow e$). In the diffraction pattern taken at e in Fig. 1, peaks from solid deuterium (phase I) appeared at around 200 K (Extended Data Fig. 2), which is consistent with the known melting curve of hydrogen²². This observation indicates that fluid deuterium coexisted with C₂ through the path from b to d .

The C₂ phase persisted at pressures at least as low as 0.5 GPa on decompression at 100 K (path $e \rightarrow f$). However, surprisingly, the Bragg peaks of C₂ mostly disappeared at 0.2 GPa (Fig. 3). This phenomenon is totally unexpected, because the host structure of gas hydrates retains its framework in the previous cases with ice XVI¹¹ and XVII¹². The sample was further decompressed to 0 GPa and evacuated using a turbo-molecular-pump. The broad peaks corresponding to ice Ic appeared at this stage. The peak disappearance of C₂ before the appearance of ice Ic was reproducibly observed in at least two separate neutron runs and one x-ray diffraction run for a hydrogenated sample (Extended Data Fig. 2). In the neutron diffraction pattern at 0.2 GPa, except for the Bragg peaks from Mg(OD)₂, only a broad peak was observed at around $d = 3.75$ Å, which was between the peak positions of 111 of C₂ and that of Ice Ic (Fig. 3). This fact implies that this state does not have long-range periodicity like a normal crystal, but has only local-ordering like an amorphous or nano-crystal. Considering the observed d -spacing, this “amorphous-like” form would be an intermediate transition state from C₂ to ice Ic, which forms while hydrogen molecules are partially degassed. It is highly likely that this apparent amorphization is derived from the lattice mismatch between C₂ and ice Ic, originating from the relatively small cage in the host framework of the ice Ic structure.

From the x-ray diffraction run, ice Ic, which may partially include molecular hydrogen, even appeared at 0.1 GPa through the transition from the C₂ phase to the “amorphous-like” state, even under pressure (Extended Data Fig. 2). This also represents a difference from the previous cases

of ice XVI and XVII; ice XVI is formed under evacuation¹¹, and hydrogen molecules can be refilled into ice XVII at an order of 10 bar of pressure¹². It is worth noting that the partially degassed states are allowed in the cases of both ice XVI and XVII, so that the guest molecules can be continuously degassed from a fully occupied state to an empty state. The observed phase-separation behavior even under pressure in the ice H₂-H₂O system indicates that the partially degassed C₂ phase would be unstable compared to the fully occupied or emptied phases, probably due to their lattice-mismatch.

The Bragg peaks in the neutron diffraction pattern for ice Ic obtained at 100 K were still broad, probably due to the small crystallite size and/or the remaining guest hydrogen molecules. The peaks of ice Ic sharpened with increasing temperature. This sharpening is dependent not only on temperature but also on time, which indicates that it is kinetic behavior.

We conducted a separate run in order to obtain a neutron diffraction pattern for the structure refinement of the ice Ic. In this run, the neutron diffraction pattern was obtained at 130 K, which is well below the temperature at which the nucleation of ice Ih occurs²³. We confirmed that the peak width did not change in the temperature region from 130 K to 180 K, such that the peak sharpening was almost complete, even at 130 K. The obtained neutron diffraction pattern was well fitted using the ice Ic structure model¹⁷, as shown in Fig. 2b and Extended Data Table 1. We also conducted the Rietveld analysis using C₂ structure model, and found that the occupancy of the D2 site was zero, within experimental error ($\text{occ}(\text{D2}) = -0.001(1)$). This shows that the guest hydrogen molecules are below the detectable limit at 130 K under evacuation. The peak profile around 111 peak of ice Ic has neither the feature of stacking-disorder nor the peaks from ice Ih, as shown in the diffraction pattern in the region at around $d = 3.9 \text{ \AA}$, where the strongest 101 reflection of ice Ih is expected (see inset in Fig. 2b, and more detailed discussion for the peak broadening for ice Ic is described in Supplementary Information). This should be a clear indication of the presence of ideal ice Ic without stacking-disorders ($\chi = 100\%$), as clear as the recent discovery of ideal ice Ic by annealing ice XVII⁹.

It is also noteworthy that the ice Ic surprisingly persists up to at least 240 K until ice Ih started

to appear at 250 K (Fig. 3). The temperature of 240 K corresponds to the upper limit of the reported metastable region of “ice Ic”¹. However, in stacking-disordered ice, the cubic stacking sequence starts to change into a hexagonal stacking sequence at a much lower temperature, and the phase transition to ice Ih is completed at 240 K. The notable stability of the ice Ic would be derived from the lack of stacking-disorder. The stacking-disordered ice has more dislocations, which promote the phase transformation from “ice Ic” to ice Ih by reducing the activation energy required to change the stacking sequence¹³. This is also supported by a recent mesoscopic-size calculation²⁴. The diffraction pattern observed at 250 K looks a mixture of bulk ice Ic and Ih, rather than stacking-disordered ice with many stacking faults, judging from “stackogram” reported in the literature^{8,18}. At 250 K, crystal growth would be dominant, rather than crystal nucleation. Therefore, once a crystallite nucleates, it quickly grows before other crystallites nucleate, resulting in the mixture of ice Ic and Ih, rather than stacking-disordered ice. This observation also suggests a smaller number of dislocations in the ice Ic observed in this study. On the contrary, the remarkable stability of the ice Ic and the bulk mixture of ice Ic and Ih at 250 K strongly supports the conclusion that the obtained ice is not stacking-disordered, and it can therefore be called ice Ic without the need for quotation marks.

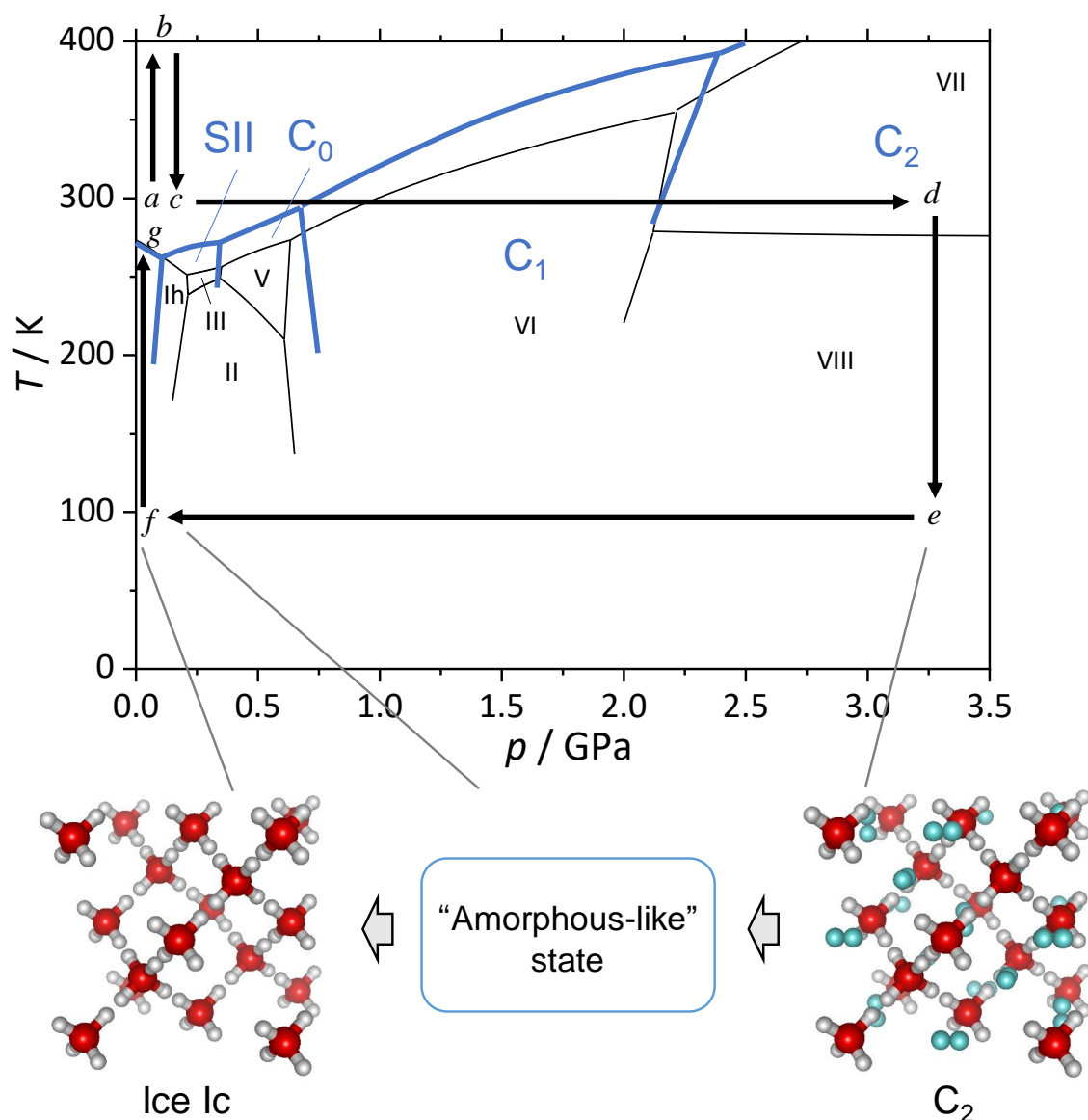


Figure 1 | Phase diagram of hydrogen hydrate and ice with experimental paths in this study.

Phase boundaries for hydrogen hydrates and ices are drawn using thick blue lines and thin black lines, respectively. Experimental p - T paths are shown as black arrows in alphabetical sequence from a to g . The structural models for a high-pressure form of hydrogen hydrate, C_2 , and ice Ic are schematically drawn with a newly found “amorphous-like” state as an intermediate transitional state from C_2 to ice Ic. Red, white, and blue balls in the structure model depict oxygen, hydrogen in water molecules, and hydrogen in guest molecules, respectively.

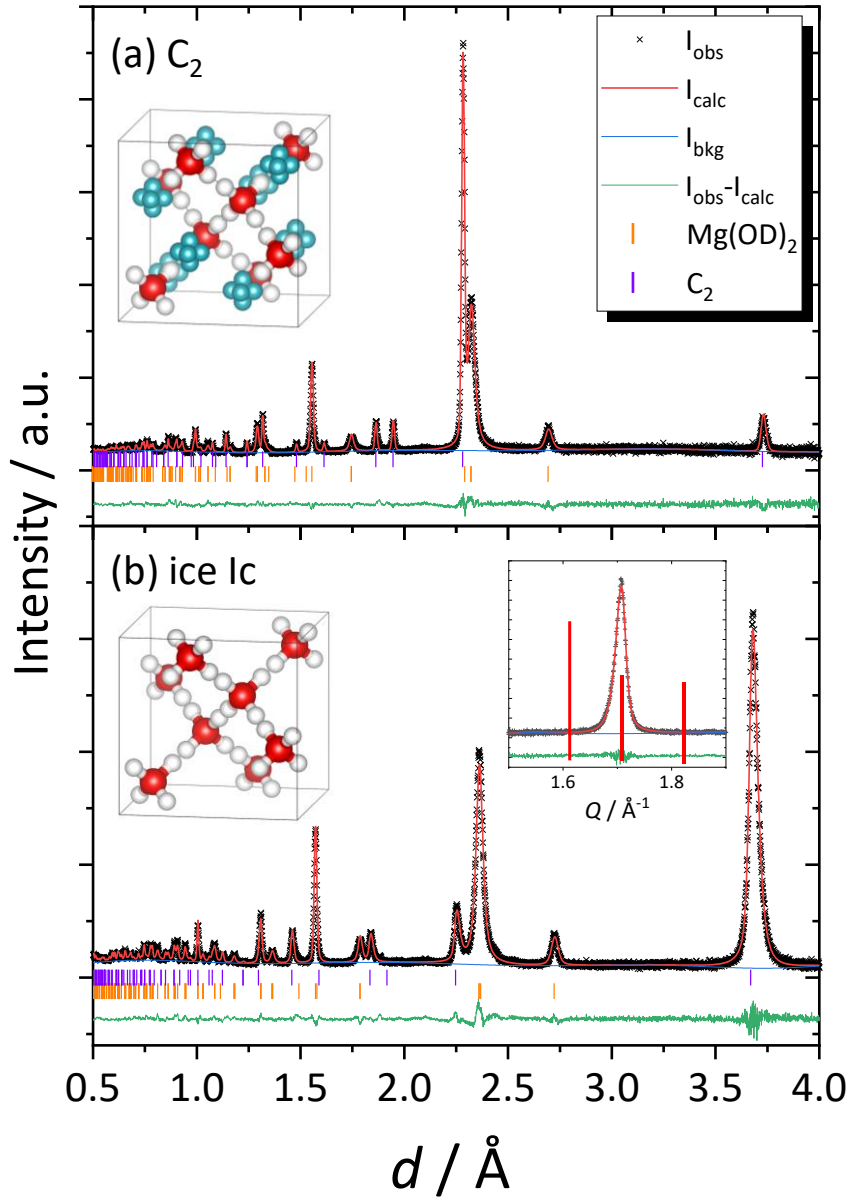


Figure 2 | Results of Rietveld analyses for neutron diffraction patterns of (a) hydrogen hydrate, C₂, and (b) ice Ic. The patterns of C₂ and ice Ic were obtained at 3.3 GPa and 300 K (at d in Fig. 1), and at 0 GPa and 130 K (in the path $f \rightarrow g$). The inset diffraction pattern in (b) shows the expanded area for 111 reflections. The calculated peak positions of ice Ih are shown as red lines in the inset. Structure models for C₂ and ice Ic are also shown as insets in (a) and (b), respectively.

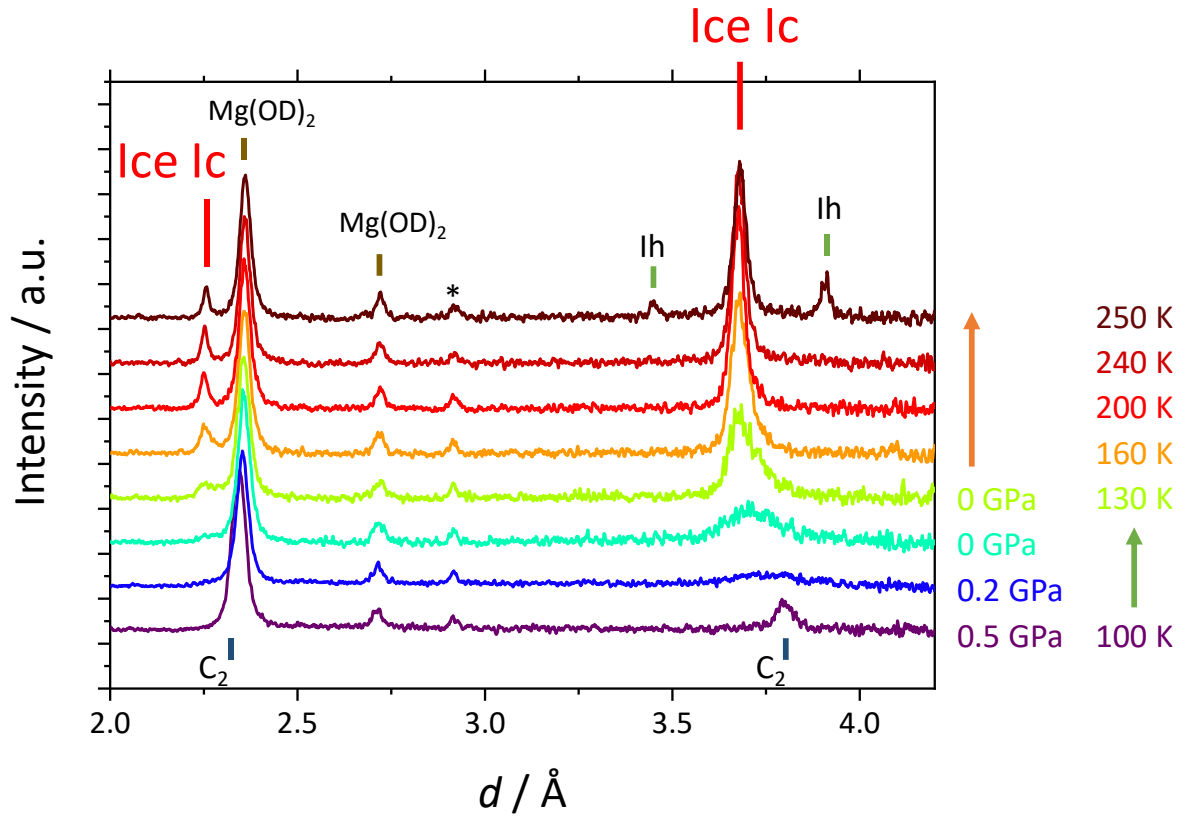


Figure 3 | Neutron diffraction patterns with decreasing pressure at 100 K (path $e \rightarrow f$) and with increasing temperature at 0 GPa (path $f \rightarrow g$). Corresponding temperatures and pressures are shown at the right side of the respective patterns. Most observed peaks are identified as C₂, ice Ic, Mg(OD)₂, or ice Ih. The peak marked by an asterisk is a parasitic peak from the high-pressure cell.

References

1. Kuhs, W. F., Sippel, C., Falenty, A. & Hansen, T. C. Extent and relevance of stacking disorder in “ice Ic”. *Proc. Nat. Acad. Sci.* **109**, 21259-21264 (2012).
2. Murphy, D. M. Dehydration in cold clouds is enhanced by a transition from cubic to hexagonal ice. *Geophys. Res. Lett.* **30**, 2230 (2003).
3. Riikonen, M. *et al.* Halo observations provide evidence of airborne cubic ice in the Earth’s atmosphere. *Appl. Opt.* **39**, 6080-6085 (2000).
4. Whalley, E. Scheiner's halo: evidence for ice Ic in the atmosphere. *Science* **211**, 389-390 (1981).
5. Gronkowski, P. The search for a cometary outbursts mechanism: a comparison of various theories. *Astronomische Nachrichten: Astronomical Notes* **328**, 126-136 (2007).
6. Prialnik, D. & Bar-Nun, A. Crystallization of amorphous ice as the cause of comet P/Halley's outburst at 14 AU. *Astron. Astrophys.* **258**, L9-L12 (1992).
7. König, H. Eine kubische Eismodifikation. *Z. Kristallogr. Cryst. Mater.* **105**, 279 (1943).
8. Malkin, T. L. *et al.* Stacking disorder in ice I. *Phys. Chem. Chem. Phys.* **17**, 60-76 (2015).
9. del Rosso, L. *et al.* Cubic ice Ic free from stacking defects synthesized from ice XVII. *arXiv preprint arXiv:1907.02915* (2019).
10. Vos, W. L., Finger, L. W., Hemley, R. J. & Mao, H.-k. Novel H₂-H₂O clathrates at high pressures. *Phys. Rev. Lett.* **71**, 3150-3153 (1993).
11. Falenty, A., Hansen, T. C. & Kuhs, W. F. Formation and properties of ice XVI obtained by emptying a type sII clathrate hydrate. *Nature* **516**, 231-233 (2014).
12. del Rosso, L., Celli, M. & Ulivi, L. New porous water ice metastable at atmospheric pressure obtained by emptying a hydrogen-filled ice. *Nat. Commun.* **7**, 13394 (2016).
13. Hondoh, T. Dislocation mechanism for transformation between cubic ice Ic and hexagonal ice Ih. *Philos. Mag.* **95**, 3590-3620 (2015).
14. Lupi, L. *et al.* Role of stacking disorder in ice nucleation. *Nature* **551**, 218 (2017).
15. Amaya, A. J. *et al.* How Cubic Can Ice Be? *J. Phys. Chem. Lett.* **8**, 3216-3222 (2017).
16. Malkin, T. L., Murray, B. J., Brukhno, A. V., Anwar, J. & Salzmann, C. G. Structure of ice crystallized from supercooled water. *Proc. Nat. Acad. Sci.* **109**, 1041-1045 (2012).
17. Kuhs, W. F., Bliss, D. V. & Finney, J. L. High-resolution neutron powder diffraction study of ice-Ic. *J. Phys.* **48**, 631-636 (1987).
18. Hansen, T. C., Sippel, C. & Kuhs, W. F. Approximations to the full description of stacking disorder in ice I for powder diffraction. *Zeitschrift für Kristallographie* **230**, 75-86 (2015).
19. del Rosso, L. *et al.* Refined structure of metastable ice XVII from neutron diffraction measurements. *J. Phys. Chem. C* **120**, 26955-26959 (2016).
20. Donnelly, M. E., Teeratchanan, P., Bull, C. L., Hermann, A. & Loveday, J. S. Ostwald's rule of stages and metastable transitions in the hydrogen–water system at high pressure. *Phys. Chem. Chem. Phys.* **20**, 26853-26858 (2018).

21. Komatsu, K. *et al.* Development of a new P–T controlling system for neutron-scattering experiments. *High. Press. Res.* **33**, 208-213 (2013).
22. Diatschenko, V. *et al.* Melting curves of molecular hydrogen and molecular deuterium under high pressures between 20 and 373 K. *Phys. Rev. B* **32**, 381-389 (1985).
23. Hansen, T. C., Koza, M. M., Lindner, P. & Kuhs, W. F. Formation and annealing of cubic ice: II. Kinetic study. *J. Phys.: Condens. Matter* **20**, 285105 (2008).
24. Chan, H. *et al.* Machine learning coarse grained models for water. *Nat. Commun.* **10**, 379 (2019).

Acknowledgments

We are grateful to Drs. J. Abe and K. Funakoshi for their assistance with the experiments. Neutron diffraction experiments were performed through the J-PARC user programs (Nos. 2014B0187, 2015A0033, 2017A0092, 2017B0031). This study was supported by JSPS KAKENHI (Grant Numbers: 18H05224, 18H01936, 15H05829).

Author contributions

KK and SM conceived and designed the experiments. KK, SM, TH, ASF, RY, KY, and HK conducted the neutron diffraction experiments. KK, RY, KY, and HK conducted the x-ray diffraction experiments. FN carried out the DFT calculations and wrote the corresponding part of the manuscript. KK analyzed the data and wrote the manuscript with contributions from all authors.

Methods

Synthesis of MgD₂

MgD₂, used as the starting material in this study, was synthesized from reagent-grade MgH₂ as follows. MgH₂ powder (Wako pure chemical industries, Ltd.) was purchased and further ground in an agate motor to increase the surface area, after which it was placed in a copper tube with a diameter of 4 mm and a length of 40 mm. The tube was mechanically sealed and but not welded, allowing the transfer of hydrogen gas. The copper tube was inserted into a 1/4" Inconel tube and connected in parallel to a deuterium gas cylinder and a turbo molecular pump (TMP) with 1/16" stainless tubes and stop bulbs. The Inconel tube, including the sample copper tube, was heated to 773 K for 1 h using a tube furnace under evacuation using the TMP. Under these conditions, MgH₂ completely decomposed to Mg and H₂²⁵, and the degassed H₂ was evacuated. Then, the D₂ gas was introduced up to 4 MPa, and the temperature was cycled at the rate of 1 K/min between 673 K and 773 K while keeping the pressure at 4 MPa, which represents stable and unstable conditions for MgH₂²⁵, and this temperature cycle was repeated for 20 times. This ‘activation’ process is necessary for the reaction $\text{Mg} + \text{D}_2 \rightarrow \text{MgD}_2$. Finally, the p - T conditions were maintained at 673 K and 4 MPa for 3 days to complete the reaction. The recovered sample was analyzed by powder x-ray diffraction (MiniFlex-II, Rigaku) and identified to be MgD₂ with a trace amount of MgO. Both MgD₂ and MgO react with D₂O and produce Mg(OD)₂, so this small amount of MgO does not affect the conclusion.

Neutron diffraction and p - T control

Neutron diffraction experiments were conducted at the beamline PLANET²⁶ in the Material and Life Science Experiment Facility (MLF) of J-PARC, Ibaraki, Japan. Approx. 20 mg of MgD₂, synthesized as described above, was filled into TiZr null scattering gaskets, and D₂O water (99.9 %, Wako pure chemical industries, Ltd.) was dropped on the MgD₂ powder, resulting in the molar ratio of MgD₂:D₂O ~ 1:3. The gaskets were sandwiched between a pair of tungsten carbide anvils, and loaded by using a “hybrid Mito system”, which is a modified version of an original pressure-temperature variable “Mito system²¹”. The hybrid Mito system uses both flowing liquid nitrogen and a 4 K cryostat (RDK-415D, Sumitomo Heavy Industries, Ltd.), which allows us to control temperature rapidly, owing to the large latent heat of liquid nitrogen and efficient thermal insulation by zirconia and GFRP seats. The hybrid Mito system also allows us to achieve temperatures below 77 K, and reach a minimum temperature of approximately 35 K, owing to the cryostat. Another remarkable feature of the hybrid Mito system is that it affords

pressure control, even at low temperature, as well as the original Mito system, which is indispensable for this study. Flexible copper cloths were attached on the support rings of the anvils, and the cloths were placed in contact with the cold head of the cryostat for thermal conduction. The accessible minimum temperature of the hybrid Mito system is ~ 35 K, which may be the current technical limitation due to an unavoidable influx of heat from the surrounding cell. The sample pressure was estimated from the observed lattice parameter of $\text{Mg}(\text{OD})_2$ brucite using the equation of states²⁷ and the observed unit cell volume of brucite at 0 GPa, assuming the temperature derivative of the bulk modulus of brucite, dK/dT , was approximately 0. Although this assumption may cause some error in the pressure estimated at low temperature, we placed emphasis on avoiding unwanted Bragg peaks from additional sources of pressure. Moreover, the error would be too small to affect the conclusion. The sample position was aligned by scanning to maximize the sample scattering intensity. The Rietveld analyses were performed using the GSAS²⁸ with EXPGUI²⁹, and the crystal structure was drawn with the VESTA program³⁰. Detailed procedures for data reduction and refinements are described elsewhere³¹.

X-ray diffraction

Powder x-ray diffraction measurements using a H_2O (Milli Q) and MgH_2 (Wako pure chemical industries, Ltd.) mixture as starting materials were performed at the beamline BL-18C in the Photon Factory (KEK, Tsukuba, Japan). Samples were exposed to 0.6134 Å monochromatized synchrotron radiation, and the diffracted scattering was detected by an imaging plate (IP). Details of data reduction procedures for x-ray diffraction are described elsewhere²¹. The pressure was generated using CuBe alloy diamond-anvil cells and the temperature was controlled using a 4K GM cryostat (MiniStat, Iwatani Co.) equipped with a temperature controller (Model 335, Lakeshore). Sample pressure was estimated from the difference in the R1 line wavelengths of rubies inside and outside the sample chamber³². The temperature was monitored using a Si-diode sensor inserted in the cold head edge. We confirmed that the measured temperature was almost the same as that of the diamond anvils after temperature stabilization. The experimental p - T path was basically identical to the case of neutron diffraction, as shown in Fig. 1, while the achieved pressure at path d was 4.1 GPa.

One conically shaped Boehler-Almax type diamond anvil³³ with a 0.6 mm culet was placed in the direction of the detector with an opening angle of $20^\circ < 40^\circ$, whereas a conventional anvil with a 0.8 mm culet was positioned in the direction of the x-ray source. A CuBe plate with a hole of diameter 0.3 mm and an initial thickness of 0.2 mm was used as a gasket. This gasket was not

subjected to pre-indentation. The load was applied by driving the piston by bellows using a He gas cylinder. The bellows allow us to control pressure at a few kbar more precisely than conventionally used membranes.

DFT calculations

Quantum Espresso³⁴ was used for the DFT calculations^{35,36}. We used Perdew-Burke-Ernzerhof (so-called PBE) type nonempirical exchange-correlation functions³⁷ for this study. The pseudopotentials were derived using projector augmented-wave approximation³⁸. The dispersion effects were taken into account using the exchange-hole dipole moment method (XDM), which calculates coefficients for polynomial of DFT-D dispersion energy³⁹ from the exchange-hole dipole moment calculated from simulated electron wave function^{40,41}. XDM damping function parameters are taken from⁴². The enthalpies of four possible configurations for the ordered form of ice Ic were calculated within a unit cell with a kinetic energy cutoff of 70 Ry and a Brillouin zone k mesh of $8 \times 8 \times 8$. The cell and atomic parameters were optimized using BFGS quasi-Newtonian methods at atmospheric pressure.

25. Crivello, J.-C. *et al.* Review of magnesium hydride-based materials: development and optimisation. *Appl. Phys. A* **122**, 97 (2016).
26. Hattori, T. *et al.* Design and performance of high-pressure PLANET beamline at pulsed neutron source at J-PARC. *Nucl. Instr., Meth. Phys. Res. A* **780**, 55-67 (2015).
27. Horita, J., dos Santos, A. M., Tulk, C. A., Chakoumakos, B. C. & Polyakov, V. B. High-pressure neutron diffraction study on H–D isotope effects in brucite. *Phys. Chem. Miner.* **37**, 741-749 (2010).
28. Larson, A. & Von Dreele, R. General Structure Analysis System (GSAS). *Los Alamos National Laboratory, Report LAUR-86-748* (2004).
29. Toby, B. EXPGUI, a graphical user interface for GSAS. *J. Appl. Crystallogr.* **34**, 210-213 (2001).
30. Momma, K. & Izumi, F. VESTA 3 for three-dimensional visualization of crystal, volumetric and morphology data. *J. Appl. Crystallogr.* **44**, 1272-1276 (2011).
31. Komatsu, K. *et al.* Crystal structure of magnesium dichloride decahydrate determined by X-ray and neutron diffraction under high pressure. *Acta. Crystallogr. B* **71**, 74-80 (2015).
32. Piermarini, G. J., Block, S., Barnett, J. D. & Forman, R. A. Calibration of the pressure dependence of the R₁ ruby fluorescence line to 195 kbar. *J. Appl. Phys.* **46**, 2774-2780 (1975).
33. Boehler, R. & De Hantsetters, K. New anvil designs in diamond-cells. *High. Press. Res.* **24**, 391-396 (2004).
34. Paolo, G. *et al.* QUANTUM ESPRESSO: a modular and open-source software project for quantum simulations of materials. *J. Phys.: Condens. Matter* **21**, 395502 (2009).

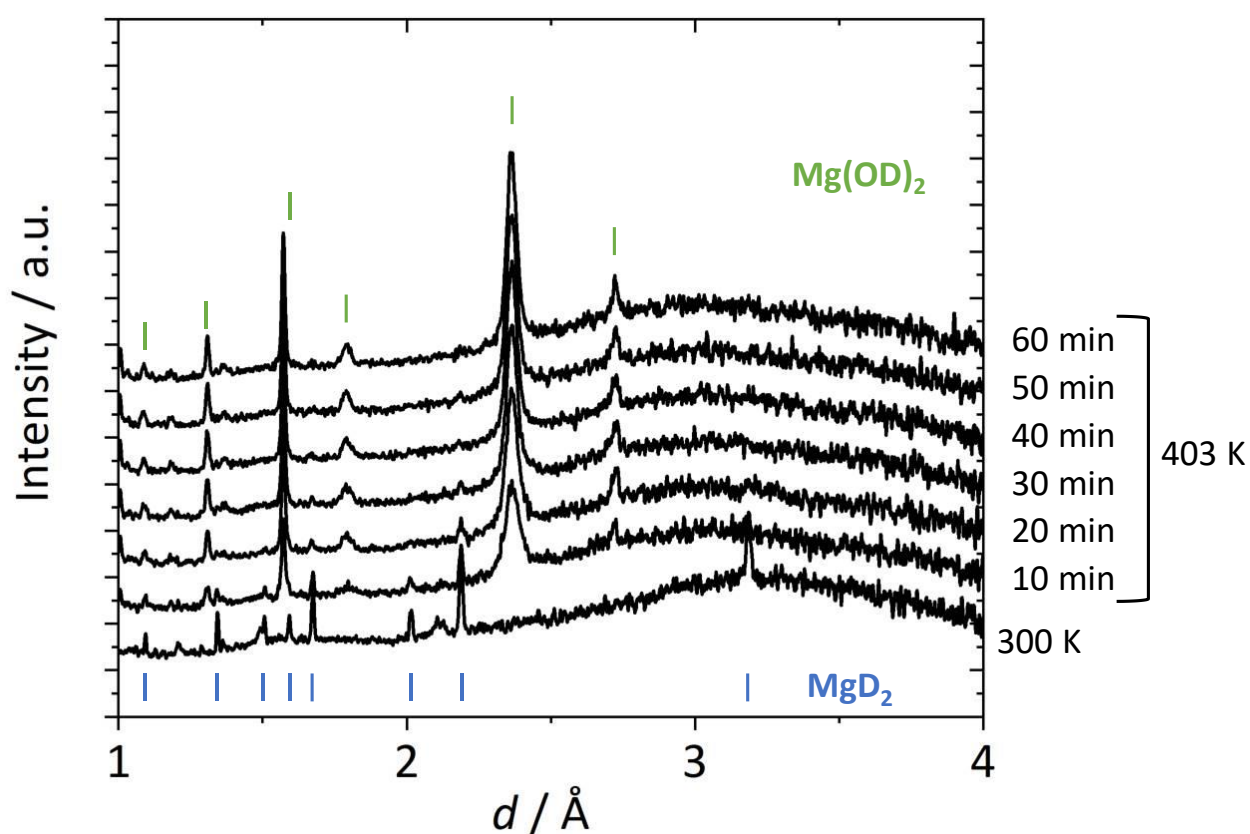
35. Hohenberg, P. & Kohn, W. Inhomogeneous Electron Gas. *Phys. Rev.* **136**, B864-B871 (1964).
36. Kohn, W. & Sham, L. J. Self-consistent equations including exchange and correlation effects. *Phys. Rev.* **140**, A1133-A1138 (1965).
37. Perdew, J. P., Burke, K. & Ernzerhof, M. Generalized Gradient Approximation Made Simple. *Phys. Rev. Lett.* **77**, 3865-3868 (1996).
38. Kresse, G. & Joubert, D. From ultrasoft pseudopotentials to the projector augmented-wave method. *Phys. Rev. B* **59**, 1758-1775 (1999).
39. Grimme, S., Antony, J., Ehrlich, S. & Krieg, H. A consistent and accurate ab initio parametrization of density functional dispersion correction (DFT-D) for the 94 elements H-Pu. *J. Chem. Phys.* **132**, 154104 (2010).
40. Becke, A. D. & Johnson, E. R. Exchange-hole dipole moment and the dispersion interaction. *J. Chem. Phys.* **122**, 154104 (2005).
41. Becke, A. D. & Johnson, E. R. Exchange-hole dipole moment and the dispersion interaction revisited. *J. Chem. Phys.* **127**, 154108 (2007).
42. Otero-de-la-Roza, A. & Johnson, E. R. Van der Waals interactions in solids using the exchange-hole dipole moment model. *J. Chem. Phys.* **136**, 174109 (2012).
43. Geiger, P. *et al.* Proton Ordering of Cubic Ice Ic: Spectroscopy and Computer Simulations. *J. Phys. Chem. C* **118**, 10989-10997 (2014).

Extended Data Table 1 | Experimental details and refined crystallographic data for C₂ and ice Ic.

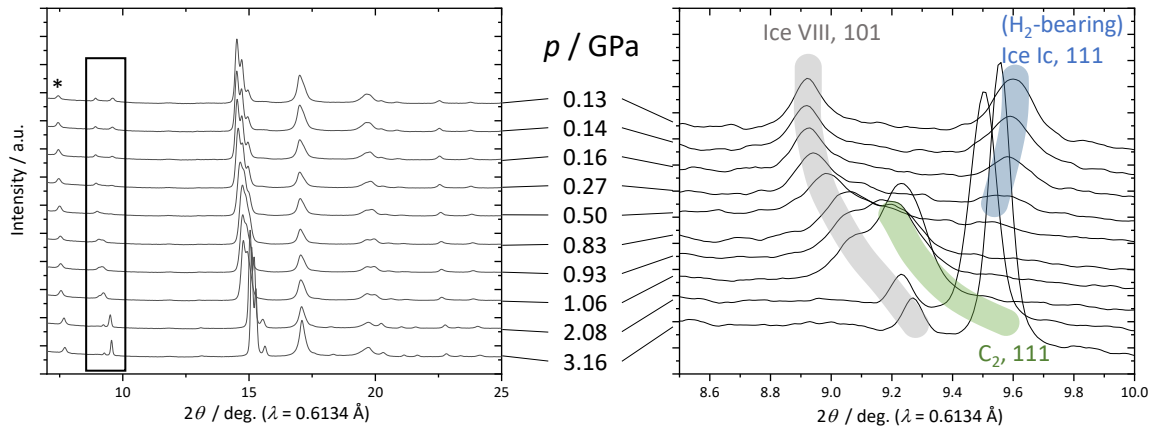
	C ₂	Ice Ic
Chemical formula	D ₂ ·D ₂ O	D ₂ O
Molecular weight	40.055	20.028
Crystal system	Cubic	Cubic
Space group	<i>Fd3̄m</i>	<i>Fd3̄m</i>
Temperature (K)	300	100
Pressure (GPa)	3.3	0
a (Å)	6.45307(8)	6.3560(2)
V (Å ³)	268.719(11)	256.77(3)
Z	8	8
Radiation type	Spallation neutron	
Diffractometer	PLANET (BL11), MLF, J-PARC	
Specimen mounting	Pressure-temperature controlling system (the hybrid MITO system)	
<i>R</i> _p	0.0379	0.0532
<i>R</i> _{wp}	0.0425	0.0605
<i>R</i> (<i>F</i> ²)	0.114	0.0772
χ^2	1.975	2.556
No. of data points	3525	3525
No. of parameters	29	24
<i>U</i> _{iso} (O)	0.0113(7)	0.0181(7)
<i>x</i> (D1 [*])	0.4607(2)	0.4675(3)
occ(D1 [*])	0.5 (fixed)	0.5 (fixed)
<i>U</i> _{iso} (D1 [*])	0.0250(9)	0.0239(7)
<i>x</i> (D2 ^{**})	0.0636(5)	-
occ(D2 ^{**})	0.310(1)	-
<i>U</i> _{iso} (D2 ^{**})	0.0250(9)	-
	(= <i>U</i> _{iso} (D1))	

*D1 belongs to a water molecule in the host structure.

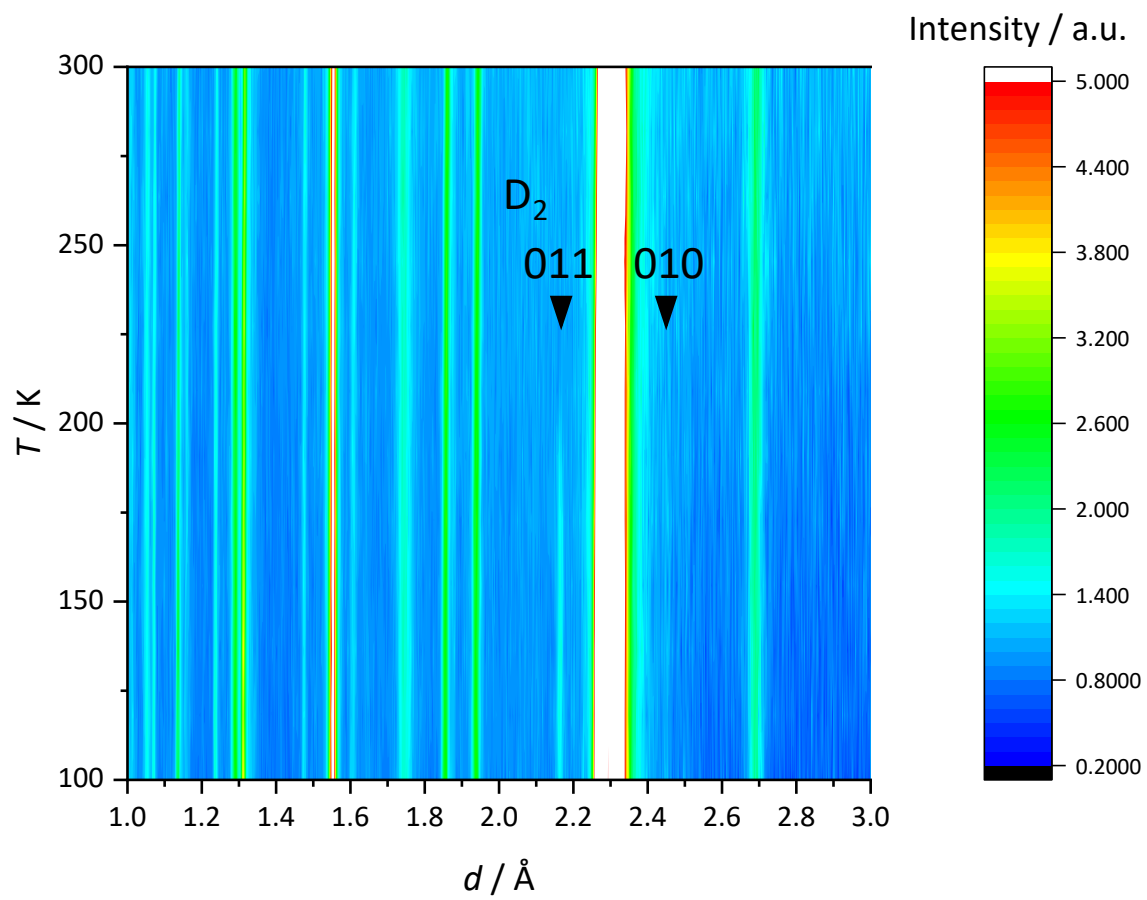
**D2 belongs to the guest deuterium molecule. *U*_{iso}(D2) is constrained to be the same value as *U*_{iso}(D1), because of the severe correlation between atomic coordinates and occupancies.



Extended Data Figure 1 | Neutron diffraction patterns for starting materials taken at 300 K (bottom, at *a* in Fig. 1), and time-resolved patterns at 403 K (at *b* in Fig. 1) for each 10 min. The obtained Bragg peaks are indexed as MgD_2 (blue tick marks) or Mg(OD)_2 (green tick marks). A broad peak at around $d \sim 3 \text{ \AA}$ in the pattern at 300 K originated from liquid D_2O , and the broad peak shifted to lower d -spacing at 403 K, which would show the existence of fluid D_2 in the sample chamber.



Extended Data Figure 2 | (a) X-ray diffraction patterns at 100 K with decreasing pressure (path $e \rightarrow f$) and (b) an enlarged 2θ region from 8.5° to 10° , corresponding to the region shown in the black box in the figure on the left. Thick blue, green, and gray lines in the figure on the right schematically show the peak positions of 111 of ice Ic and C₂, and 101 of ice VIII, respectively. Because the MgH₂:H₂O ratio in the starting material of this x-ray diffraction run was not sufficiently high to make pure C₂, ice VIII remained in this run. At 0.50 GPa, 111 peaks of both C₂ and ice Ic mostly disappeared, indicating the intermediate amorphous-like state at that pressure. The asterisk in the left figure denotes a scattering from Mylar® (polyester) film, which is used for a window material of the vacuum chamber.



Extended Data Figure 3 | Sequential neutron diffraction patterns with decreasing temperature (path $d \rightarrow e$). Two 011 and 010 peaks from solid D_2 (Phase I) are clearly seen, as shown by black triangles.

Supplementary Information

On the peak broadening of ice Ic

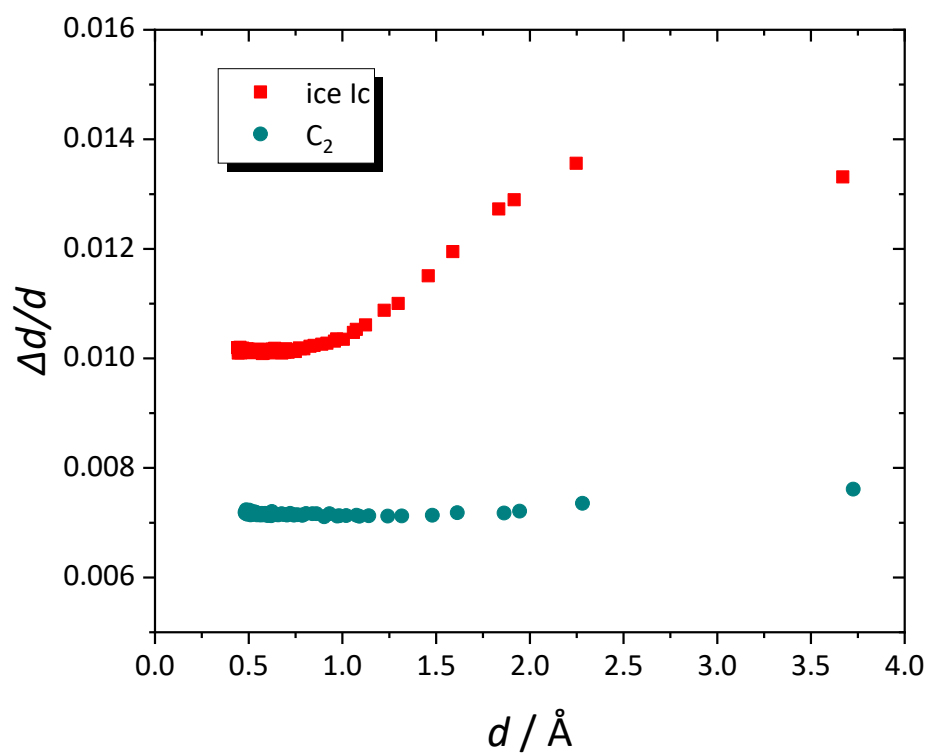
The peak width of the ice Ic obtained in this study ($\Delta d/d \sim 1.2\%$) are significantly larger than the instrument resolution ($\Delta d/d \sim 0.6\%$)²⁶, as shown in Supplementary Fig. S1. This broadening cannot be the result of stacking-disorder, because the profile changes caused by the stacking-disorder are not simply broadening, but more complicated^{8,18}. Considering the result that the peak width did not change up to 240 K once the peak sharpening converged, it is unlikely that the peak broadening of ice Ic could originate only from small crystalline size. Other broadening factors such as microstrain induced by lattice distortions should be taken into account (see also Supplementary Fig. S1). We assume the lattice distortion could be caused by proton ordering, and then conducted the DFT calculations for the ordered form of ice Ic in order to estimate the degree of lattice distortion. There are four possible symmetrically non-equivalent configurations for ice Ic with unit cell volumes identical to that of the disordered ice Ic, having the space groups of $Pna2_1$, $I4_1md$, $P4_1$, and $P4_12_12^{43}$. The optimized unit cell parameters show deviations from the cubic lattice (Supplementary Table S1). The deviation, which can be defined as the ratio of cell parameters between the characteristic axis (= the most deviated axis from cubic symmetry) and the other axes, ranges from 0.12 % for the $P4_1$ model to 1.16 % for the $P4_12_12$ model. The degree of deviation is of an order similar to the peak broadening of 0.6% (1.2 % – 0.6 %) added to the instrument resolution. Although the obtained ice Ic does not have the long-range ordering for protons, short-range ordering could result in the lattice distortion, which contributes to the peak broadening.

Supplementary Table S1 | Results of DFT calculations for four symmetrically non-equivalent ordered forms of ice Ic.

Order model	1	2	3	4
Crystal system	Orthorhombic*	Tetragonal	Tetragonal	Tetragonal
Space Group	$Pna2_1$ *	$I4_1md$	$P4_1$	$P4_12_12$
Dipole Moment (Debye)	5.64	7.96	3.95	7.65E-05
a	6.1953	6.1711	6.1806	6.1352
b	6.1953	6.2007	6.1878	6.2070
c	6.1547	6.1711	6.1806	6.2070
α	90.0000	90.0000	90.0000	90.0000
β	90.0000	90.0000	90.0000	90.0000
γ	90.0242	90.0000	90.0000	90.0000
Charac. axis /Cubic axis**	0.9935	1.0048	1.0012	0.9884
$H(\text{eV})/8\text{H}_2\text{O}$	-4799.3535	-4799.3755	-4799.3358	-4799.3249
$\Delta H(\text{eV})/8\text{H}_2\text{O}$	0.0219281	0	0.0396700	0.0505637

*DFT calculation was started from the orthorhombic $Pna2_1$ structure, but the symmetry of the optimized structure could be reduced from orthorhombic to monoclinic.

**Ratio of cell parameters between the characteristic axis and cubic axis. The characteristic axis shows the greatest deviation from the cubic axis, as shown by shades.



Supplementary Figure S1 | Full width at half maximum divided by d -spacing ($\Delta d/d$) as a function of d -spacing for C₂ and ice Ic.